Transient Absorption of Transition Metal Dichalcogenide Monolayers Studied by a Photodope-Pump-Probe Technique

Pavel Valencia-Acuna,¹ Peymon Zereshki,¹ Mohammad Mahdi
Tavakoli,² Ji-Hoon Park,² Jing Kong,² and Hui Zhao^{1,*}

¹Department of Physics and Astronomy, The University of Kansas,

Lawrence, Kansas 66045, United States

²Department of Electrical Engineering and Computer Science,

Massachusetts Institute of Technology,

Cambridge, Massachusetts 02139, United States

(Dated: June 23, 2020)

Abstract

We report three-pulse photodope-pump-probe measurements on photocarrier dynamics in semiconducting transition metal dichalcogenide monolayers of MoS₂, WS₂, MoSe₂, and WSe₂. The samples are fabricated by chemical vapor deposition and mechanical exfoliation techniques and characterized by photoluminescence spectroscopy. In the time-resolved measurement, the samples are first photodoped by a prepulse, which injects background photocarriers of various densities. A pump pulse then excites photocarriers, whose dynamics is monitored by measuring differential reflection of a time-delayed probe pulse. We found that the ultrafast decay component of the differential reflection signal, which has been widely reported before, shows minimal dependence on the background exciton density. This observation shows that a previously suggested carrier-trapping model cannot account for this component. The results thus further support an exciton-formation model that was previously proposed based on spectroscopic evidence.

I. INTRODUCTION

The discovery of graphene¹ has created an exponentially growing interest in a whole family of two-dimensional (2D) materials². Semiconducting transition metal dichalcogenides (TMDs), as a promising group of 2D materials, have been extensively studied since 2010. These TMDs, such as MoS₂, WS₂, MoSe₂, and WSe₂, possess several interesting properties. For example, their monolayer forms have direct bandgaps in the visible range, although their bulk and multilayer counterparts are all indirect semiconductors^{3,4}. Their unique lattice structure enables valley-selective optical coupling⁵, which can be utilized in valleytronics. Their 2D structure with reduced dielectric screening results in unusually large exciton binding energies^{6,7}, making them ideal platforms to study excitonic physics and many-body interactions. Because of these superior properties, they are regarded as promising materials for the next-generation and ultrathin optoelectronic devices^{8,9}.

Photocarrier dynamics is an important process in semiconductors that often determines the performance of optoelectronic devices based on them. As such, the photocarrier dynamics in 2D TMDs has been extensively studied, mostly by using pump-probe techniques based on transient absorption. In a typical pump-probe experiment, an ultrashort laser pulse (pump) injects photocarriers, which lifecycle is time-resolved by measuring the transient absorption of a probe pulse as a function of the time delay between the two pulses. By using this technique and its variations, significant progress has been made on understanding several important aspects of the photocarrier dynamics in TMDs and other 2D semiconductors, such as thermalization¹⁰, energy relaxation^{10–12}, exciton-exciton annihilation^{13–18}, exciton diffusion^{19–24} and recombination^{13,15,16,22,25–36}, spin and valley dynamics^{26,27,37–50}, and coherent exciton processes^{51,52}.

In transient absorption measurements of 2D TMDs, one commonly observed feature is an ultrafast decay process that causes loss of about half of the signal in about 1 ps. This feature is remarkably consistent across different TMDs studied, including MoS₂^{11,25,53,54}, WS₂^{27,28,55,56}, MoSe₂²⁴, and WSe₂²², with samples fabricated by different groups and with different techniques. This process shows no apparent dependence on the temperature²⁷ or the dielectric environment²⁴ of the samples. Understanding the physical origin of this process is important for using the pump-probe technique to study photocarrier dynamics, especially those occurring on ultrafast time scales.

So far, three models have been proposed on the origin of this ultrafast decay process, based on exciton-exciton annihilation^{11,29,53}, extrinsic effects of defect states^{25,29,31,54,57}, and the intrinsic effect of exciton formation⁵⁸. At first, it has been established that in 2D semiconductors, the

exciton-exciton annihilation can be significantly more efficient than in 3D systems due to the enhanced exciton-exciton interaction^{13–18}. Thus, at elevated densities, the exciton-exciton annihilation can cause rapid loss of the exciton population, resulting in the ultrafast decay of the transient absorption^{11,29,53}. Second, lattice defects in the samples can cause loss of photocarriers by trapping or defect-assisted Auger-type recombination, which can dominate carrier dynamics at low densities and cause this ultrafast decay process^{25,29,31,54,57}. Finally, the intrinsic effect of exciton formation from free electron-hole pairs have been proposed as a possible mechanism of the ultrafast decay process⁵⁸.

Here we utilize a three-pulse photodope-pump-probe technique to study the origin of the ultrafast decay process in MoS₂, WS₂, MoSe₂, and WSe₂ at low carrier density regimes by testing the hypothesis of the defect-trapping mechanism. We use a prepulse to optically dope the samples, followed by injection of photocarriers by a pump pulse and measurement of differential reflection of a probe pulse. If the trapping of carriers by defects is the main mechanism for this ultrafast decay process, the carriers injected by the prepulse are expected to fill these states and thus suppress or even eliminate this component. Our measurements over a large range the photodoping densities in all four materials show that the ultrafast decay process is not influenced by photodoping. The results thus prove that the defect-related processes are not responsible for the ultrafast decay process observed in these samples, suggesting the importance of the contributions from exciton formation.

II. EXPERIMENTAL TECHNIQUE AND PROCEDURES

MoS₂ monolayer samples are synthesized by metal-organic chemical vapor deposition on Si/SiO₂ substrates under low pressures. The precursors for Mo and S, molybdenum hexacarbonyl (98 %, Sigma Aldrich) and diethyl sulfide (98 %, Sigma Aldrich), respectively, are supplied in a gaseous phase by a bubbler system. The flow rates for argon, molybdenum hexacarbonyl, and diethyl sulfide are 100, 0.6, and 2.0 sccm, respectively. The growth lasted for 15 h at a substrate temperature of 400°C. Monolayer samples of WS₂, MoSe₂, and WSe₂ are fabricated by a standard mechanical exfoliation technique. For each material, flakes are first peeled off from a bulk crystal (purchased from 2D Semiconductor) by an adhesive tape, and then transferred to a polydimethyl-siloxane (PDMS) substrate. Under an optical microscope, the substrate is examined to identify large monolayer regions, based on their known optical contrasts on such thick and transparent

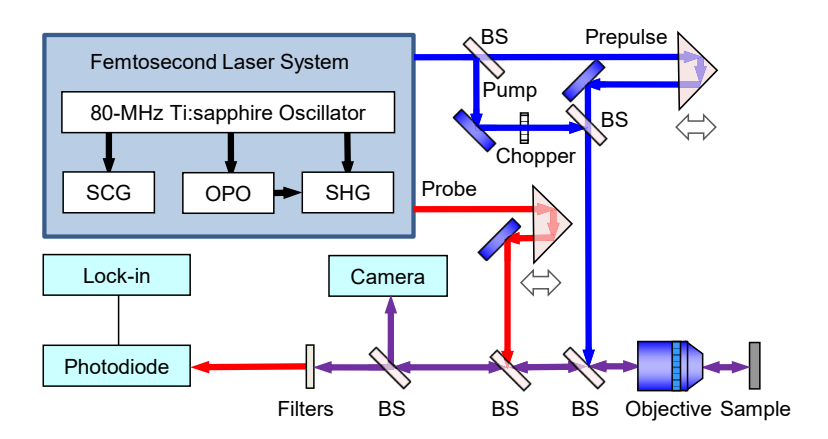


FIG. 1. Schematics of the three-pulse photodope-pump-probe setup.

substrates⁵⁹. The identified monolayers are transferred to a Si/SiO₂ (90 nm) substrate to facilitate optical measurements. The inclusion of samples fabricated by different techniques could provide information on to what degree the results are influenced by the fabrication techniques.

The photodope-pump-probe measurements were performed in the reflection geometry with a home-made setup, as schematically shown in Figure 1. The laser system includes an 80-MHz Ti:sapphire oscillator, an optical parametric oscillator (OPO), a supercontinuum generator (SCG), and a second harmonic generation (SHG) unit. The Ti:sapphire oscillator produces 100-fs pulses in the range of 700 - 900 nm. One part of this output is guided into the photonic-crystal fiber SCG, which generates a coherent and broadband irradiation. A bandpass filter (with a bandwidth of 10 nm) is used to select the desired wavelength component for the experiment. Another part of the Ti:sapphire output pumps the OPO, which produces near infrared pulses that are converted to visible light by SHG in a nonlinear crystal. The output of the Ti:sapphire oscillator can also produce its second harmonic directly by the SHG unit, or be directly used.

In a measurement, depending on the desired wavelength range, one of these outputs (blue beam in Figure 1) is split by a beamsplitter (BS) and is used as the prepulse and the pump pulse. The former is sent to a retroreflector and then combined with the latter by another BS. By moving the retroreflector on a linear stage, the path length (and therefore the time delay) of the prepulse with respect to the pump pulse can be adjusted. The combined prepulse/pump are reflected by a BS to a microscope objective lens, which focuses them to the sample. Typical spot sizes are in the range of $1 - 2 \mu m$. A mechanical chopper is used to modulate the pump intensity at about 3 kHz. Another output of the laser system is used as the probe (red beam in Figure 1). It is sent to another retroreflector for time-delay adjustment, and is focused to the sample by the same objective lens.

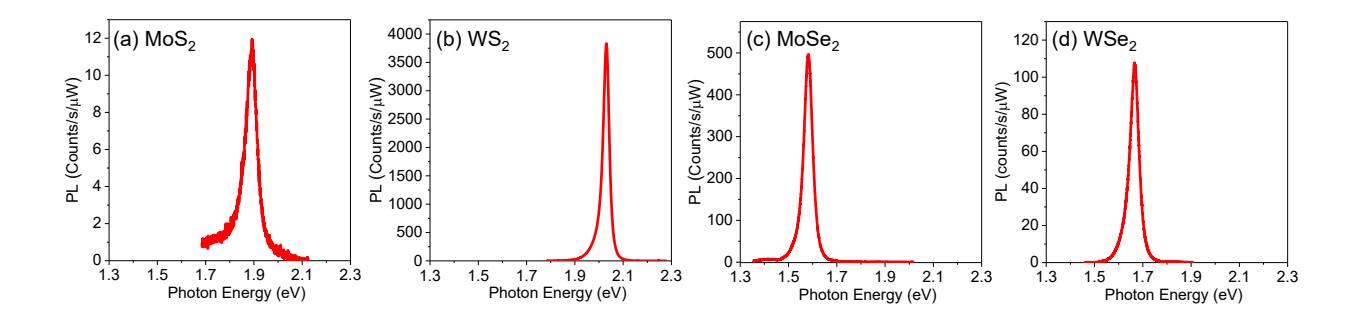


FIG. 2. Room-temperature photoluminescence spectra of monolayers of MoS₂ (a), WS₂ (b), MoSe₂ (c), and WSe₂ (d) under the continuous-wave excitation of 3.06 eV.

The reflected probe from the sample (purple beam in Figure 1) is collected by the objective lens and goes through the BS's. A camera monitors the focused spots and the sample surface during the alignment process. A filter is used to block the unwanted prepulse/pump reflection, allowing only the probe to reach the photodiode, which voltage output is measured by a lock-in amplifier that is referenced by the chopping frequency.

With this setup, we use the prepulse to photodope the sample prior to the arrival of the pump at the sample, and then measure the differential reflection of the probe induced by the pump, $\Delta R/R_0 = (R-R_0)/R_0$. Here, R and R_0 are the reflectance of the sample with and without the presence of the pump beam, respectively; however, they are both with the presence of the prepulse. It is important to note that the carriers injected by the prepulse alter both R and R_0 by the same amount and therefore do not influence $\Delta R/R_0$: Since only the pump beam is modulated by the chopper and the lock-in amplifier measures the signal at that modulation frequency, only the differential reflection induced by the pump-injected carriers is detected. All the measurements were performed with the samples at room temperature and under ambient condition.

III. RESULTS AND DISCUSSION

The samples were first characterized by photoluminescence (PL) spectroscopy. Figure 2 shows the room temperature PL spectra of the four samples under the excitation of a continuous-wave laser with a photon energy of 3.06 eV. The PL intensities plotted are normalized against the integration time and the excitation power; hence, their comparison approximately reflects the relative PL yields of these samples. As shown in Figure 2, the normalized PL count varies from about 12 in MoS₂ to over 3500 in WS₂. Furthermore, the observed PL yields, the peak positions, and

the peak widths are all consistent with previously reported results from the corresponding TMD monolayers⁵⁹, confirming the monolayer thickness of the samples.

Figure 3 schematically shows our approach to study photocarrier dynamics in the photodoped TMD monolayers. At first, a prepulse injects electron-hole pairs in a TMD monolayer at -4 ps (a). That is, the prepulse arrives at the sample 4-ps before the pump pulse. This time is long enough for the completion of the carrier thermalization, energy relaxation, and exciton formation processes, but is short enough so that the loss of photocarriers due to recombination is negligible. Figure 3(b) illustrates this situation right before the arrival of the pump pulse, where a thermalized exciton population with a temperature being equal to the lattice temperature (293 K) is established. As hypothesized, some of the photocarriers could be lost to the trap states. Next (c), the pump pulse arrives at the sample at t = 0, injecting more carriers in the now photodoped sample. The dynamics of these carriers is monitored by measuring the differential reflection of a probe pulse that is tuned to the excitonic resonance (d). The key observation is that, if the trapping of carriers was responsible for the ultrafast decay component of the transient absorption signal, the carriers injected by the prepulse would occupy these states, causing reduction or even elimination of this component in the transient absorption associated with the pump-injected carriers, which can no longer been trapped.

Since the probe is tuned to the exciton resonance of the sample [Figure 3(d)], one might assume that it only senses excitons. However, this assumption is invalid. It has been well established through early studies on excitons in semiconductor quantum wells that free electron-hole pairs can also saturate the exciton oscillator strength. This is because the exciton wave function is composed of free-carrier states; hence, occupation of these states can alter the excitonic oscillator strength through the phase-space state filling effect⁶⁰. In fact, when their thermal energy is much smaller than the exciton binding energy (a condition that is typically fulfilled in 2D semiconductors due to their large exciton binding energies), the free electron-hole pairs can alter the absorption at the excitonic resonance even more efficiently than an exciton population of the same density⁶⁰.

We first perform standard pump-probe measurements with either the prepulse or the pump pulse exciting the sample along, to confirm their effectiveness of injecting carriers and their optimal alignment. The red circles in Figure 4 show the differential reflection signal measured from the WS₂ monolayer sample, as an example. In this measurement, the prepulse was blocked and the pump pulse was modulated by the chopper. The photon energies of the pump and probe are 3.12 and 2.01 eV, respectively. The signal reaches the peak rapidly, followed by an ultrafast decay to

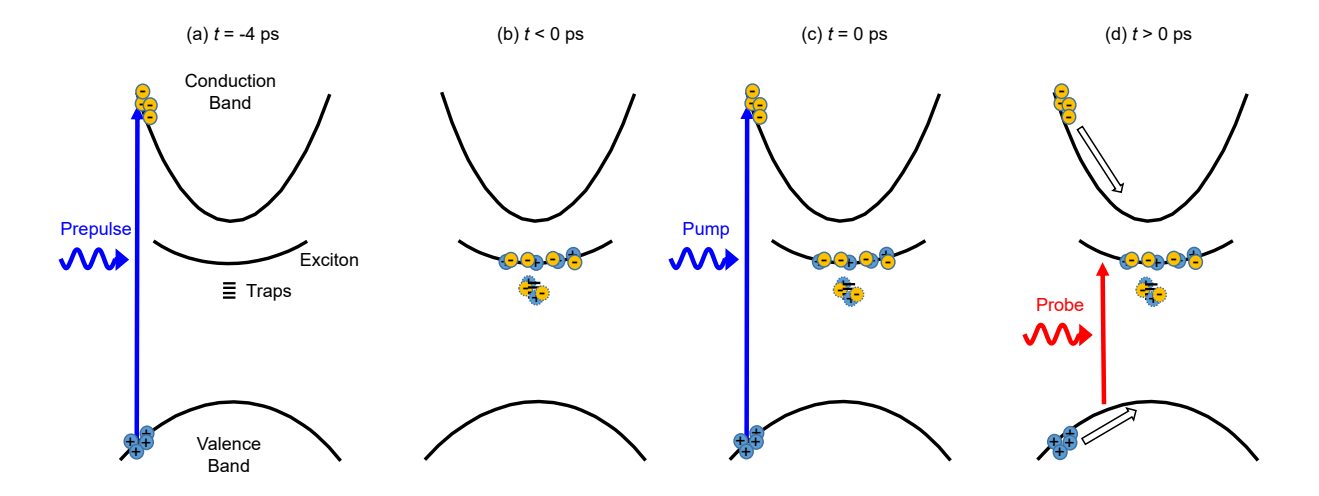


FIG. 3. Schematics of the photocarrier injection and dynamics. (a) A prepulse excites electrons (solid circles with -) and holes (+) at -4 ps. (b) The electron-hole pairs excited by the prepulse thermalize and form excitons. Some of the carriers might be captures by the trap states (dashed circles). (c) At t = 0 ps, a pump pulse injects electron-hole pairs again to the photodoped sample. (d) The dynamics of the pump-injected photocarriers is monitored by a probe pulse tuned to the exciton resonance.

about 40 % of its peak value. We next block the pump pulse and use the chopper to modulate the prepulse. The blue squares in Figure 4 show the measured differential reflection signal. The similarity of the two signals confirms that all three laser spots are well overlapped. The 4-ps separation of the two signals is well expected, as illustrated in the top panel of Figure 4. In the entire study, such a calibration measurement is always performed first, to ensure the proper alignment of the three pulses and the effectiveness of photodoping.

Figure 5 shows the results of our photodope-pump-probe measurements on the monolayer samples of MoS₂ (a), WS₂ (b), MoSe₂ (c), and WSe₂ (d). For each sample, we first measure its differential reflection signal as a function of the probe photon energy. The photon energies that give the maximal signals are 1.87, 2.01, 1.58, and 1.68 eV for MoS₂, WS₂, MoSe₂, and WSe₂, respectively. These probe photon energies are then used for the rest of the study. The pump photon energy is 3.12 eV for all the samples except MoSe₂, which is pumped by 1.97 eV due to the limitations of the laser configuration. However, in each sample, the pump photon energy is large enough to inject free electron-hole pairs⁵⁸.

We first focus on the results from MoS₂. The black squares in Figure 5(a) show the differential reflection signal with the prepulse blocked. The 3.12-eV pump with a peak fluence of $0.6 \mu J \text{ cm}^{-2}$

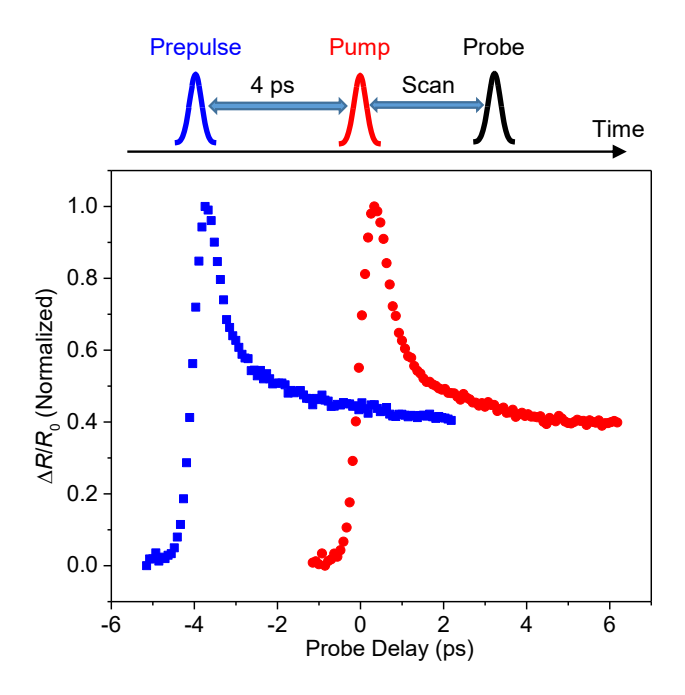


FIG. 4. Differential reflection signal of WS_2 monolayer under the excitation of the pump (red circles) or the prepulse (blue squares) alone, with the other pulse blocked. The photon energy of the prepulse and the pump pulse is 3.12 eV. The probe photon energy is 2.01 eV.

produces a differential reflection signal of the 1.87-eV probe on the order of 3×10^{-4} . Using an absorption coefficient of 1.5×10^8 m⁻¹ at the pump photon energy⁶¹, the peak injected carrier density (at the center of the pump spot) is about 1.1×10^{11} cm⁻². The average distance between the electron-hole pairs or excitons is about 30 nm, much larger than the exciton Bohr radius of a few nm. We use such a low injection density for this study so that multi-exicton processes, such as exciton-exciton annihilation, can be ignored. As shown in Figure 5(a), the signal reaches a peak quickly. The rising part of the signal can be fit by the integral of a Gaussian function with a width (full width at half maximum) of 0.5 ps, as shown by the gray curve. This temporal width is close to the width of the cross correlation of the pump and probe pulses, both of which are about 0.3 ps due to the dispersive elements of the setup (mainly the objective lens). Hence, the pump-injected carriers (in the form of free electron-hole pairs) induced the maximal differential reflection signal at the A-exciton resonance on a time scale shorter than the time resolution of the setup. This feature has been generally observed in TMD monolayers in previous studies discussed in Introduction. After the peak, the signal rapidly decays to about 50 % of its peak value. This feature is the main goal of the present study.

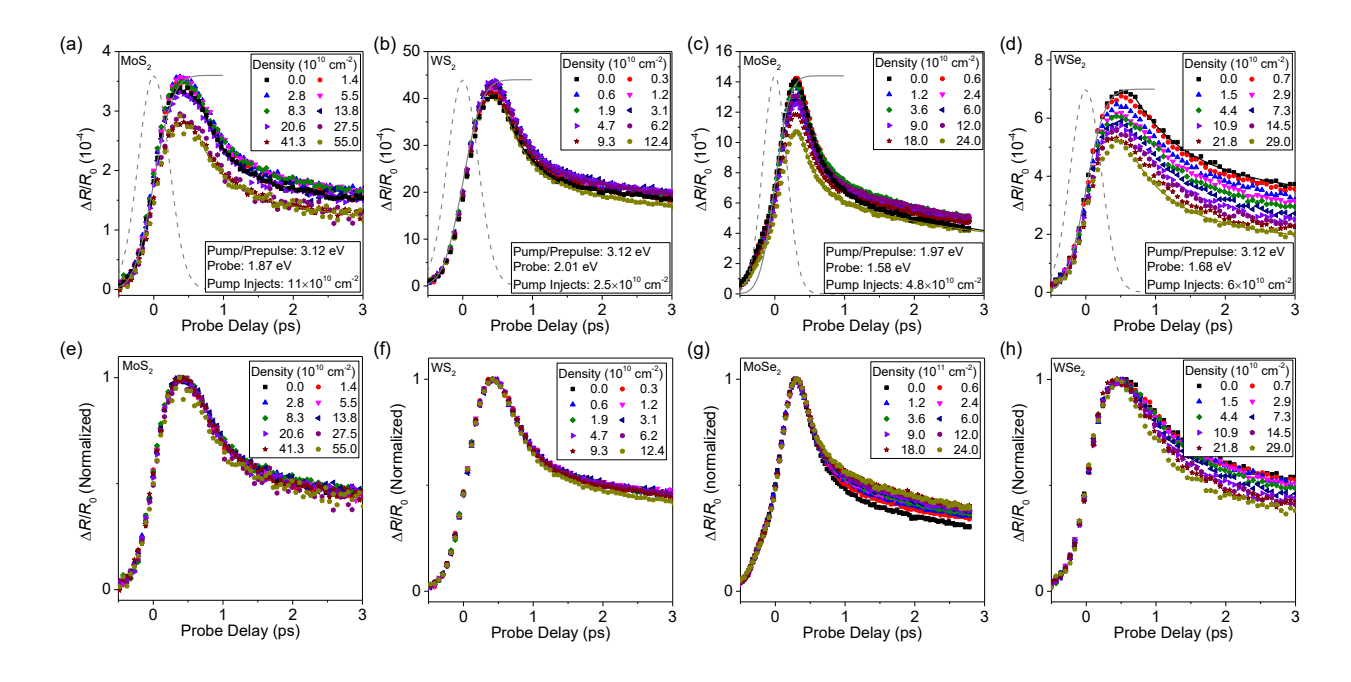


FIG. 5. Differential reflection signal measured with the photodope-pump-probe technique from the TMD monolayers of MoS_2 (a), WS_2 (b), $MoSe_2$ (c), and WSe_2 (d), respectively. Different symbols represent results with different background exciton densities injected by the prepulse. Other experimental conditions are labeled in each panel. The sample is at room temperature. (e) - (h) are the same from (a) - (d) but are normalized to shown their similarity.

We can exclude any direct nonlinear interactions between the pump and the probe pulses as the origin of the ultrafast decay component, such as sum frequency generation, SHG, or nondegenerate two-photon absorption. Such processes only occur when the two pulses overlap, while this component clearly persists far beyond the pulses. To illustrate this, the dashed gray curve is the calculated cross correlation of the pump and probe pulses, which is significantly narrower.

As we discussed above, one possible origin of the ultrafast decay process proposed was the loss of carriers due to defects in the sample. Hypothetically, if the main mechanism responsible for the loss of carriers is defect-assisted Auger-type carrier recombination, without carriers occupying these states, the entire carrier population should be drained by this process. The existence of the long-lived signal (of tens to hundreds of picoseconds) generally observed after the ultrafast decay process could rule out this mechanism. In other words, the observation that these defects can cause ultrafast decay of part of the carrier population, and then become inactive to the remaining carrier population shows that the only plausible mechanism is the trapping of carriers by these states. That is, once these states are filled, they no longer cause decay of the carrier population.

To test this hypothesis, we use the prepulse to produce background excitons, so that these traps can be prefilled. The different symbols in Figure 5(a) shows the differential reflection signal measured when the prepulse injects various densities of background excitons, as indicated in the label. When the background density produced by the prepulse is comparable to or higher than the maximal carrier density that these states can capture (which is about half of the pump injected density, or about 0.5×10^{11} cm⁻², based on the trapping mechanism), the ultrafast decay component should be significantly quenched. However, as shown in Figure 5(a), even with the background exciton densities up to 10 times higher than the pump-injected density, the ultrafast decay component is nearly unaffected. This can be clearly seen in Figure 5(e), which show the normalized signals. Similar results were obtained from the other three TMD monolayers, as shown in the rest of Figure 5. Hence, these results rule out the trapping mechanism. Furthermore, the close similarity of this feature in all four TMDs samples studied, which are fabricated with different techniques, strongly suggest an intrinsic and universal origin of this ultrafast decay process.

In a previous study, we have shown spectroscopic evidence that such an ultrafast decay component is not associated with loss of carrier population and that it only exists under nonresonant excitation of free electron-hole pairs⁵⁸. Based on these features, we proposed that this process is associated with formation of excitons from the free electron-hole pairs⁵⁸. This explanation is also consistent with a well-established model on transient absorption of semiconductor quantum wells, which predicted that under the conditions relevant to 2D TMDs at room temperature, free electron-hole pairs induce transient absorption at the excitonic resonance that is twice of that induced by excitons of the same density⁶⁰. By ruling out the trapping mechanism, the result of photodope-pump-probe experiment provides strong evidence supporting this model. We note that our experimental observations do not imply lack of effects of defects on the photocarrier dynamics and the optical response of TMD monolayers. To the contrary, defects are known to significantly reduce the photocarrier lifetime by providing nonradiative recombination channels⁶². Our study merely shows that their effects on ultrafast time scales are miner and they are not responsible for the generally observed ultrafast decay process.

We now discuss some detailed observations from the results shown in Figure 5 that are not strongly related to our conclusion. First, the peak signal decreases slightly at high background densities in each sample. To better illustrate that, the top panels of Figure 6 show the peak signal as a function of the background density for each sample. This feature could be attributed to the effect of absorption saturation. That is, the differential reflection is related to the exciton density by

 $\Delta R/R_0 = AN/(N+N_s)$, where N_s is the saturation density⁶². Although the background excitons do not directly contribute to the signal detected, as their density is not modulated, they still contribute to this saturation effect. Second, we characterize the magnitude of this fast-decay component by taking the ratio between the signal at 3 ps to the peak signal. This ratio is plotted in the middle panels of Figure 6. As shown in Panels (a) and (b), this ratio is in the range of 0.4 - 0.5 and is independent of the background density in MoS_2 and WS_2 monolayers. For the other two samples, however, the ratio slightly increases (MoS_2) and decreases (WS_2) with the background density. Finally, the decay times deduced by exponential fits to this component (curves in Figure 5) are shown in the bottom panels of Figure 6. Small variations from material to material can be seen, while the background-density dependence is rather weak.

The time scale of exciton formation based on this model is consistent with previous studies with other techniques. If the ultrafast decay process is due to exciton formation, the decay times shown in the bottom panels of Figure 6 correspond to the exciton formation times in these materials, ranging from 0.3 ps (MoSe₂) to 0.7 ps (WSe₂). Previous time-resolved mid-infrared spectroscopic measurement also reported sub-picosecond exciton formation time in monolayer WSe₂⁶³. In WS₂, ultrafast decay of THz conductivity on similar time scales was attributed to the exciton formation process^{64,65}. Recently, this ultrafast decay component has been utilized to tune the exciton binding

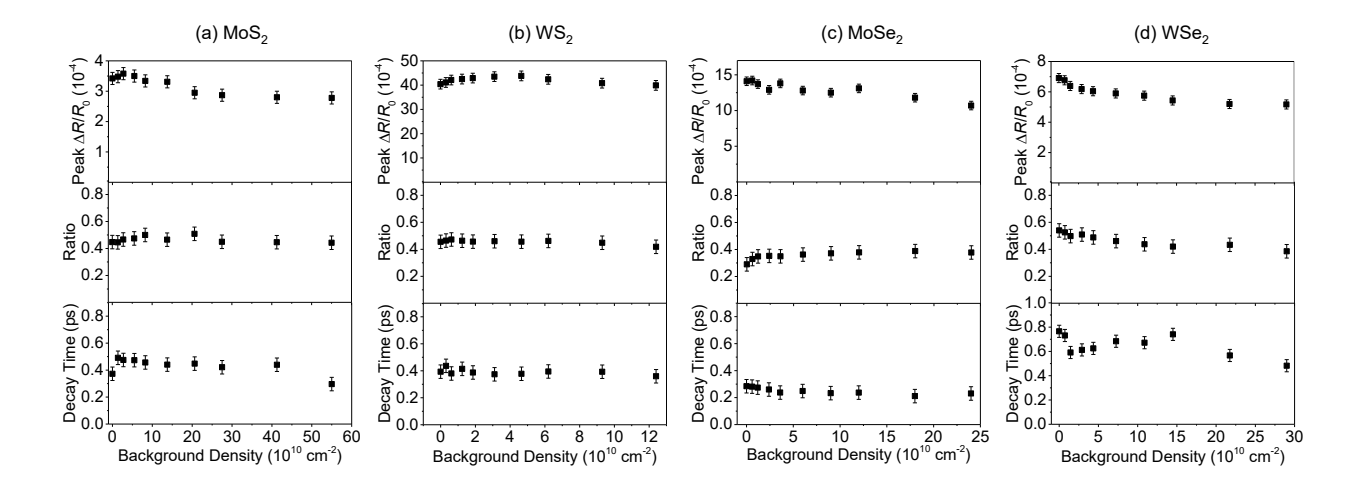


FIG. 6. Parameters describing the ultrafast decay component of the differential reflection signal shown in Figure 5 from monolayers of MoS₂ (a), WS₂ (b), MoSe₂ (c), and WSe₂ (d), respectively. the top panels are the peak differential reflection signal. The middle panels show the ratio of the differential reflection signal at 3 ps to the peak signal, that is, the amount of the signal drop due to the ultrafast decay component. The bottom panels are the decay time constants as a function of the background exciton density.

energy of WS₂ by photoexcitation based on the exciton-formation model⁵⁵. We also note that once an exciton is formed, it can capture an additional charge carrier to form a trion⁶⁶. A previous study has shown that in MoSe₂ this trion formation time is about 2 ps⁶⁷. Hence, trion formation process, which happens after excitons are formed, is not expected to impact this ultrafast decay process. Furthermore, the decay of the differential reflection signal reflects the loss of free electron-hole pair population, which could be due to the formation of both bright and dark excitons. Hence, the exciton formation times deduced here include both types of exciton formation process.

IV. CONCLUSION

We have performed three-pulse photodope-pump-probe experiments on monolayer semiconductors of MoS₂, WS₂, MoSe₂, and WSe₂. Under nonresonance excitation conditions, an ultrafast decay process of the transient absorption was observed in all materials, with similar decay time constants and weights to the overall signal magnitude. We show that this component is independent of the background exciton density injected by the prepulse over a large density range. This result shows that a previously hypothesized photocarrier trapping mechanism is not the main origin of this component observed in our samples. This observation further supports the model of exciton formation.

V. ACKNOWLEDGEMENT

The authors acknowledge the financial support of National Science Foundation of USA (DMR-1505852), KU Research Go and Research Excellence Initiative Award, and the U. S. Army Research Office through the Institute for Soldier Nanotechnologies at MIT, under Cooperative Agreement No. W911NF-18-2-0048.

¹ K. S. Novoselov, A. K. Geim, S. V. Morozov, D. Jiang, Y. Zhang, S. V. Dubonos, I. V. Grigorieva, and A. A. Firsov, Science **306**, 666 (2004).

^{*} huizhao@ku.edu

² Z. Lin, A. McCreary, N. Briggs, S. Subramanian, K. H. Zhang, Y. F. Sun, X. F. Li, N. J. Borys, H. T. Yuan, S. K. Fullerton-Shirey, A. Chernikov, H. Zhao, S. McDonnell, A. M. Lindenberg, K. Xiao, B. J.

- LeRoy, M. Drndic, J. C. M. Hwang, J. Park, M. Chhowalla, R. E. Schaak, A. Javey, M. C. Hersam, J. Robinson, and M. Terrones, 2D Mater. 3, 042001 (2016).
- ³ K. F. Mak, C. Lee, J. Hone, J. Shan, and T. F. Heinz, Phys. Rev. Lett. **105**, 136805 (2010).
- ⁴ A. Splendiani, L. Sun, Y. Zhang, T. Li, J. Kim, C. Y. Chim, G. Galli, and F. Wang, Nano Lett. **10**, 1271 (2010).
- ⁵ D. Xiao, G. B. Liu, W. Feng, X. Xu, and W. Yao, Phys. Rev. Lett. **108**, 196802 (2012).
- ⁶ A. Chernikov, T. C. Berkelbach, H. M. Hill, A. Rigosi, Y. L. Li, O. B. Aslan, D. R. Reichman, M. S. Hybertsen, and T. F. Heinz, Phys. Rev. Lett. **113**, 076802 (2014).
- ⁷ K. He, N. Kumar, L. Zhao, Z. Wang, K. F. Mak, H. Zhao, and J. Shan, Phys. Rev. Lett. **113**, 026803 (2014).
- ⁸ B. Radisavljevic, A. Radenovic, J. Brivio, V. Giacometti, and A. Kis, Nat. Nanotechnol. **6**, 147 (2011).
- ⁹ B. Radisavljevic and A. Kis, Nat. Mater. **12**, 815 (2013).
- ¹⁰ Z. Nie, R. Long, L. Sun, C. C. Huang, J. Zhang, Q. Xiong, D. W. Hewak, Z. Shen, O. V. Prezhdo, and Z. H. Loh, ACS Nano 8, 10931 (2014).
- ¹¹ L. Wang, Z. Wang, H. Y. Wang, G. Grinblat, Y. L. Huang, D. Wang, X. H. Ye, X. B. Li, Q. L. Bao, A. S. Wee, S. A. Maier, Q. D. Chen, M. L. Zhong, C. W. Qiu, and H. B. Sun, Nat. Commun. 8, 13906 (2017).
- ¹² Z. Chi, H. L. Chen, O. Zhao, and Y. X. Weng, Nanotechnology **31**, 235712 (2020).
- ¹³ N. Kumar, O. Cui, F. Ceballos, D. He, Y. Wang, and H. Zhao, Phys. Rev. B **89**, 125427 (2014).
- ¹⁴ D. Sun, Y. Rao, G. A. Reider, G. Chen, Y. You, L. Brezin, A. R. Harutyunyan, and T. F. Heinz, Nano Lett. 14, 5625 (2014).
- ¹⁵ L. Yuan and L. B. Huang, Nanoscale **7**, 7402 (2015).
- ¹⁶ C. Poellmann, P. Steinleitner, U. Leierseder, P. Nagler, G. Plechinger, M. Porer, R. Bratschitsch, C. Schuller, T. Korn, and R. Huber, Nat. Mater. 14, 889 (2015).
- ¹⁷ Y. L. Yu, Y. F. Yu, C. Xu, A. Barrette, K. Gundogdu, and L. Y. Cao, Phys. Rev. B **93**, 201111 (2016).
- ¹⁸ V. Pareek, J. Madeo, and K. M. Dani, Phys. Rev. Lett. **124**, 057403 (2020).
- ¹⁹ B. A. Ruzicka, S. Wang, L. K. Werake, B. Weintrub, K. P. Loh, and H. Zhao, Phys. Rev. B 82, 195414 (2010).
- ²⁰ J. He, D. He, Y. Wang, O. Cui, M. Z. Bellus, H.-Y. Chiu, and H. Zhao, ACS Nano **9**, 6436 (2015).
- ²¹ R. Wang, B. A. Ruzicka, N. Kumar, M. Z. Bellus, H.-Y. Chiu, and H. Zhao, Phys. Rev. B **86**, 045406 (2012).
- ²² O. Cui, F. Ceballos, N. Kumar, and H. Zhao, ACS Nano **8**, 2970 (2014).

- ²³ Q. Cui, J. He, M. Z. Bellus, M. Mirzokarimov, T. Hofmann, H.-Y. Chiu, M. Antonik, D. He, Y. Wang, and H. Zhao, Small **11**, 5565 (2015).
- ²⁴ S. Hao, M. Z. Bellus, D. H. Y. Wang, and H. Zhao, Nanoscale Horiz. **5**, 139 (2020).
- ²⁵ H. Shi, R. Yan, S. Bertolazzi, J. Brivio, B. Gao, A. Kis, D. Jena, H. G. Xing, and L. Huang, ACS Nano 7, 1072 (2012).
- ²⁶ Q. Wang, S. Ge, X. Li, J. Qiu, Y. Ji, J. Feng, and D. Sun, ACS Nano 7, 11087 (2013).
- ²⁷ C. Mai, Y. G. Semenov, A. Barrette, Y. F. Yu, Z. H. Jin, L. Y. Cao, K. W. Kim, and K. Gundogdu, Phys. Rev. B 90, 041414 (2014).
- ²⁸ J. He, D. He, Y. Wang, Q. Cui, F. Ceballos, and H. Zhao, Nanoscale **7**, 9526 (2015).
- ²⁹ C. J. Docherty, P. Parkinson, H. J. Joyce, M. H. Chiu, C. H. Chen, M. Y. Lee, L. J. Li, L. M. Herz, and M. B. Johnston, ACS Nano 8, 11147 (2014).
- ³⁰ T. Yan, X. Qiao, X. Liu, P. Tan, and X. Zhang, Appl. Phys. Lett. **105**, 101901 (2014).
- ³¹ H. N. Wang, C. J. Zhang, and F. Rana, Nano Lett. **15**, 8204 (2015).
- M. Seo, H. Yamaguchi, A. D. Mohite, S. Boubanga-Tombet, J. C. Blancon, S. Najmaei, P. M. Ajayan, J. Lou, A. J. Taylor, and R. P. Prasankumar, Sci. Rep. 6, 21601 (2016).
- W. B. Gao, L. Huang, J. L. Xu, Y. Q. Chen, C. H. Zhu, Z. H. Nie, Y. Li, X. F. Wang, Z. D. Xie, S. N. Zhu, J. Xu, X. G. Wan, C. Zhang, Y. B. Xu, Y. Shi, and F. Q. Wang, Appl. Phys. Lett. 112, 171112 (2018).
- ³⁴ H. N. Wang, C. J. Zhang, W. M. Chan, C. Manolatou, S. Tiwari, and F. Rana, Phys. Rev. B 93, 045407 (2016).
- ³⁵ P. Zereshki, Y. Q. Wei, F. Ceballos, M. Z. Bellus, S. D. Lane, S. D. Pan, R. Long, and H. Zhao, Nanoscale 10, 11307 (2018).
- ³⁶ X. F. Wang, K. Shinokita, H. E. Lim, N. B. Mohamed, Y. Miyauchi, N. T. Cuong, S. Okada, and K. Matsuda, Adv. Funct. Mater. 29, 1806169 (2019).
- ³⁷ C. Mai, A. Barrette, Y. Yu, Y. G. Semenov, K. W. Kim, L. Cao, and K. Gundogdu, Nano Lett. **14**, 202 (2013).
- ³⁸ S. Dal Conte, F. Bottegoni, E. A. A. Pogna, D. De Fazio, S. Ambrogio, I. Bargigia, C. D'Andrea, A. Lombardo, M. Bruna, F. Ciccacci, A. C. Ferrari, G. Cerullo, and M. Finazzi, Phys. Rev. B 92, 235425 (2015).
- ³⁹ N. Kumar, J. He, D. He, Y. Wang, and H. Zhao, Nanoscale **6**, 12690 (2014).

- 40 C. R. Zhu, K. Zhang, M. Glazov, B. Urbaszek, T. Amand, Z. W. Ji, B. L. Liu, and X. Marie, Phys. Rev. B 90, 161302 (2014).
- ⁴¹ W. T. Hsu, Y. L. Chen, C. H. Chen, P. S. Liu, T. H. Hou, L. J. Li, and W. H. Chang, Nat. Commun. **6**, 8963 (2015).
- ⁴² L. Y. Yang, N. A. Sinitsyn, W. B. Chen, J. T. Yuan, J. Zhang, J. Lou, and S. A. Crooker, Nat. Phys. 11, 830 (2015).
- ⁴³ F. Volmer, S. Pissinger, M. Ersfeld, S. Kuhlen, C. Stampfer, and B. Beschoten, Phys. Rev. B **95**, 235408 (2017).
- ⁴⁴ J. N. Huang, T. B. Hoang, T. Ming, J. Kong, and M. H. Mikkelsen, Phys. Rev. B **95**, 075428 (2017).
- ⁴⁵ E. J. Sie, C. H. Lui, Y. H. Lee, L. Fu, J. Kong, and N. Gedik, Science **355**, 1066 (2017).
- ⁴⁶ H. M. Su, A. Y. Deng, Z. H. Zhen, and J. F. Dai, Phys. Rev. B **97**, 115426 (2018).
- ⁴⁷ L. Y. Yang, W. B. Chen, K. M. McCreary, B. T. Jonker, J. Lou, and S. A. Crooker, Nano Lett. **15**, 8250 (2015).
- ⁴⁸ F. Mahmood, Z. Alpichshev, Y. H. Lee, J. Kong, and N. Gedik, Nano Lett. **18**, 223 (2018).
- ⁴⁹ Z. L. Wang, A. Molina-Sanchez, P. Altmann, D. Sangalli, D. D. Fazio, G. Soavi, U. Sassi, F. Bottegoni, F. Ciccacci, M. Finazzi, L. Wirtz, A. C. Ferrari, A. Marini, G. Cerullo, and S. D. Conte, Nano Lett. 18, 6882 (2018).
- K. Shinokita, X. F. Wang, Y. Miyauchi, K. Watanabe, T. Taniguchi, S. Konabe, and K. Matsuda, Phys. Rev. B 99, 245307 (2019).
- ⁵¹ E. J. Sie, J. W. McIver, Y.-H. Lee, L. Fu, J. Kong, and N. Gedik, Nat. Mater. **14**, 290 (2015).
- J. Kim, X. Hong, C. Jin, S. F. Shi, C. Y. Chang, M. H. Chiu, L. J. Li, and F. Wang, Science 346, 1205 (2014).
- ⁵³ S. Sim, J. Park, J.-G. Song, C. In, Y.-S. Lee, H. Kim, and H. Choi, Phys. Rev. B **88**, 075434 (2013).
- ⁵⁴ S. H. Aleithan, M. Y. Livshits, S. Khadka, J. J. Rack, M. E. Kordesch, and E. Stinaff, Phys. Rev. B **94**, 035445 (2016).
- ⁵⁵ P. D. Cunningham, A. T. Hanbicki, K. M. McCreary, and B. T. Jonker, ACS Nano 11, 12601 (2017).
- ⁵⁶ R. K. Chowdhury, S. Nandy, S. Bhattacharya, M. Karmakar, S. N. B. Bhaktha, P. K. Datta, A. Taraphder, and S. K. Ray, 2D Mater. **6**, 015011 (2019).
- ⁵⁷ H. N. Wang, C. J. Zhang, and F. Rana, Nano Lett. **15**, 339 (2015).
- ⁵⁸ F. Ceballos, Q. Cui, M. Z. Bellus, and H. Zhao, Nanoscale **8**, 11681 (2016).
- ⁵⁹ F. Ceballos, P. Zereshki, and H. Zhao, Phys. Rev. Mater. **1**, 044001 (2017).

- ⁶⁰ T. C. Damen, J. Shah, D. Y. Oberli, D. S. Chemla, J. E. Cunningham, and J. M. Kuo, Phys. Rev. B 42, 7434 (1990).
- ⁶¹ H.-L. Liu, C.-C. Shen, S.-H. Su, C.-L. Hsu, M.-Y. Li, and L.-J. Li, Appl. Phys. Lett. **105**, 201905 (2014).
- ⁶² F. Ceballos and H. Zhao, Adv. Funct. Mater. **27**, 1604509 (2017).
- P. Steinleitner, P. Merkl, P. Nagler, J. Mornhinweg, C. Schuller, T. Korn, A. Chernikov, and R. Huber, Nano Lett. 17, 1455 (2017).
- ⁶⁴ S. J. Xu, J. Yang, H. C. Jiang, F. H. Su, and Z. Zeng, Nanotechnology **30**, 265706 (2019).
- ⁶⁵ X. Xing, L. T. Zhao, Z. Y. Zhang, X. K. Liu, K. L. Zhang, Y. Yu, X. Lin, H. Y. Chen, J. Q. Chen, Z. M. Jin, J. H. Xu, and G. H. Ma, J. Phys. Chem. C 121, 20451 (2017).
- ⁶⁶ K. F. Mak, K. He, C. Lee, G. H. Lee, J. Hone, T. F. Heinz, and J. Shan, Nat. Mater. **12**, 207 (2013).
- A. Singh, G. Moody, K. Tran, M. E. Scott, V. Overbeck, G. Berghauser, J. Schaibley, E. J. Seifert, D. Pleskot, N. M. Gabor, J. Q. Yan, D. G. Mandrus, M. Richter, E. Malic, X. D. Xu, and X. Q. Li, Phys. Rev. B 93, 041401 (2016).